Insight into highly efficient simultaneous photocatalytic removal of Cr(VI) and 2,4-diclorophenol under visible light irradiation by phosphorus doped porous ultrathin g-C_3N_4 nanosheets from aqueous media: Performance and reaction mechanism

Yaocheng Deng [a,b], Lin Tang [a,b,*], Guangming Zeng [a,b,*], Zhejing Zhu [a,b], Ming Yan [a,b], Yaoyu Zhou [c], Jiajia Wang [a,b], Yani Liu [a,b], Jingjing Wang [a,b]

[a] College of Environmental Science and Engineering, Hunan University, Changsha, 410082, China
[b] Key Laboratory of Environmental Biology and Pollution Control, Hunan University, Ministry of Education, Changsha 410082, China
[c] College of Resources and Environment, Hunan Agricultural University, Changsha 410128, China

ARTICLE INFO

ABSTRACT

Carbon nitride (g-C_3N_4) has attracted great attention for its wide applications in hydrogen evolution and photocatalytic degradation. In this study, phosphorus doped porous ultrathin carbon nitride nanosheets (PCN-S) were prepared successfully via the element doping and thermal exfoliation method. The prepared PCN-S was characterized by XRD, SEM, TEM, N_2-adsorption-desorption measurement, FT-IR, XPS, UV–vis diffuse reflectance spectra, photoluminescence (PL), photocurrent response (I-t) and EIS. The results show that PCN-S owns regular crystal structure of g-C_3N_4, large specific surface areas and nanosheet structure with lots of in-plane pores on its surface, excellent chemical stability, and broad light response to the whole visible light region, which was attributed to the doping of phosphorus element. Under visible light irradiation, the photocatalytic reduction of Cr(VI) over different samples indicated that the P doping and porous nanosheet structure play an important role for the enhanced performance of PCN-S. The reason was that P element doping can broaden the visible light response region, and large specific surface areas from the porous nanosheet structure can provide quantities of active sites for the photocatalytic reaction. Then the detailed study on the PCN-S for simultaneous photocatalytic reduction of Cr(VI) and oxidation of 2,4-diclorophenol (2,4-DCP) was conducted. The experiments results show that low pH value and enough dissolved oxygen were found to promote Cr(VI) reduction and 2,4-DCP oxidation. The detailed photocatalytic mechanism was proposed. The strategies used in this study could provide new insight into the design of g-C_3N_4 based materials with high photocatalytic activity, and present potential for the treatment of Cr(VI)/2,4-DCP or other mixed pollutants in wastewater.

© 2016 Elsevier B.V. All rights reserved.

1. Introduction

In this decade, photocatalytic degradation, as an economic efficient and environmental friendly advanced oxidation processes (AOPs), has been developed rapidly and widely. Various treatment approaches have been employed in the removal of harmful environmental contaminants, such as organic dyes, antibiotics, heavy metals and phenols [1–11]. Among the heavy metal pollutants, chromium is a common contaminant and widely exists in industrial waste discharges, such as textile manufacturing, leather tanning, paint fabrication, steel fabrication, petroleum refining and so on [12–14]. Chromium mainly exists as Cr(VI) and Cr(III) in nature, and the features of these two states are very different. Cr(VI) has been demonstrated to be a highly toxic and mutagenic substance to environment and human beings [15]. However, Cr(III) is not only less harmful but also an essential trace metal in human daily life [16]. Therefore, the conversion of Cr(VI) to Cr(III) is usually considered to be an efficient method for wastewater treatment and environmental remediation. In addition to heavy metal pollutant, chlorophenols (CPs) also bring great threat to environment. Chlorophenols are widely used as flame retardants, biocides and wood treatment agents in synthetic chemistry. The wide distribution of these pollutants can cause chronic toxicity,

mutagenicity and carcinogencity [17,18]. 2,4-diclorophenol (2,4-DCP), as one of the most abundant chlorophenols, often used as an important intermediate in the production of the herbicide 2,4-dichlorophenoxyacetate (2,4-D) [19,20]. Besides, due to the serious harmful effect to environment and humans, 2,4-DCP has been listed as one of the priority pollutants by the United States EPA and has attracted great attentions [21]. So it is an urgent need to find an efficient method for the treatment and removal of 2,4-DCP in ecosystems. So far, lots of researchers have been concentrating on the photocatalytic reduction of Cr(VI) and oxidation of 2,4-DCP [20,22–24]. For example, Cui and coworkers studied the removal of Cr(VI) by 3D TiO$_2$-graphene hydrogel via adsorption enriched with photocatalytic reduction, and they also investigated the efficient removal of 2,4-DCP by a stable Ag$_3$PO$_4$@PANI core@shell hybrid [25,26]. However, most of the photocatalytic system focused on the separate reduction of Cr(VI) and degradation of 2,4-DCP. In most cases, heavy metals and organic pollutants often co-exist in industrial wastewater and natural aqueous environment, and the wastewater containing both chromium and chlorophenol can easily be found, such as tannery effluents. Some researchers have studied the simultaneous Cr(VI) reduction and 4-chlorophenol (4-CP) oxidation using TiO$_2$ based composites [27,28]. But owing to the wide band gap of the TiO$_2$, the performances and applications are greatly limited. So it is important to develop more efficient and simultaneous photocatalytic treatment methods for the treatment of these mixed pollutants [19,29,30].

During the photocatalytic process, the performance of the photocatalyst determined the removal efficiency of pollutants, and it is necessary to design and fabricate stable and efficient photocatalysts [31–33]. Recently, graphitic carbon nitride (g-C$_3$N$_4$) has been rapidly developed and widely used in photocatalytic degradation and hydrogen evolution. g-C$_3$N$_4$ owns a band gap of 2.7 eV, which means the ability for the employment of visible light [34,35]. Compared with other photocatalysts, g-C$_3$N$_4$ has been regarded as an attractive metal-free visible-light photocatalyst owing to its unique characteristics, such as easy preparation, low cost, nontoxic and chemical stability [36,37]. Although g-C$_3$N$_4$ exhibits photocatalytic ability for the degradation of organics in some content, the performance of bare g-C$_3$N$_4$ are still far from satisfactory. The reasons can be summarized as the following three aspects: (i) limited response in visible-light irradiation; (ii) fast recombination of photogenerated electron-holes; (iii) relative low specific surface area [38].

To further improve the performance of g-C$_3$N$_4$, various modification strategies have been applied, such as coupling with other semiconductor materials [39–43], doping with other elements [38,44], exfoliating into two-dimensional nanosheets [45,46], as well as structure and surface adjustment [47,48]. Among these methods mentioned above, doping with other elements, especially with non-metal elements, has been considered as an efficient way. Because this strategy plays an important role in extending the light response region, increasing the charge transfer mobility and creating more active sites [38]. To date, some researchers have reported that P-doped g-C$_3$N$_4$ performed enhanced visible-light photocatalytic activity. For example, Zhou et al. prepared brand new P-doped g-C$_3$N$_4$ and presented improved photocatalytic for H$_2$ production and Rhodamine B degradation under visible light irradiation [49]. Hu and co-authors used (NH$_4$)$_2$HPO$_4$ as the source of phosphorous to prepare phosphorous modified g-C$_3$N$_4$ and presented enhanced performance for the degradation of Rhodamine B (RhB) [50]. Although the improved performance of the P-doped g-C$_3$N$_4$ was obtained, the specific surface areas of their prepared g-C$_3$N$_4$ were still very low. To increase the specific surface area of g-C$_3$N$_4$, converting the bulk g-C$_3$N$_4$ into nanosheets has been proved to be an efficient strategy. This strategy can provide large specific surface area, abundant active sites, short charge diffusion distance and enhanced redox abilities of photogenerated electrons and holes.

However, as for two dimensional g-C$_3$N$_4$ nanosheets, there exists one inevitable problem. That is the largely increased band gap due to the strong quantum confinement effects (QCE), which seriously inhibits their photocatalytic performance and practical application for solar energy conversion [45,51]. Besides, the strategies used in these studies just solved one or two impacts of the demerits that exist in pristine g-C$_3$N$_4$. Are there methods which can help to solve the above three problem at the same time? Will g-C$_3$N$_4$ prepared by the combination of P doping and thermal exfoliation have higher photocatalytic activity? Moreover, according to other researcher's works, the photocatalytic oxidation ability and reduction ability of g-C$_3$N$_4$ have both been separately demonstrated. Will the simultaneous band gap engineering and macropores created in 2D g-C$_3$N$_4$ nanosheets have good performance in synergistic photocatalytic reduction of Cr(VI) and oxidation of 2,4-DCP?

In this study, the P doping and thermal exfoliation strategies were combined for the synthesis of whole metal-free phosphorus-doped porous ultrathin g-C$_3$N$_4$ nanosheets (PCN-S). 2-aminoethylphosphonic acid (AEP) was used as the phosphorus source and for gas production to generate in-plane pores on the surface of g-C$_3$N$_4$ nanosheets. The prepared PCN-S with broad visible light response region, limited recombination efficiency of the photogenerated electron-hole pairs and large specific surface area, was applied in the simultaneous photocatalytic reduction of Cr(VI) and oxidation of 2,4-DCP to seek enhanced performance. To obtain deeper understanding of the synergistic effect between the reduction of Cr(VI) and oxidation of 2,4-DCP, systematical experiments have been conducted, including the control experiments performed to reveal the roles of Cr(VI), 2,4-DCP and g-C$_3$N$_4$ in the oxidation and reduction process. The effects of initial substrate concentrations, pH, dissolved oxygen and hole scavengers were also studied. A synergistic reduction-oxidation mechanism was finally proposed based on the experimental results.

2. Experimental

2.1. Materials

Melamine (>98.0%), 2,4-DCP (>99%) and disodium ethylenediamine tetraacetate (EDTA-Na$_2$, AR) were purchased from Sinopharm Chemical Reagent Co., Ltd (Shanghai, China). 2-aminoethylphosphonic acid (AEP) (>99%) was purchased from Sigma-Aldrich (USA). All reagents were used as received from commercial suppliers without further purification. Deionized water (18.25 MΩ cm specific resistance) generated by an Ulupure (UPR-II-10T) laboratory water system was used to prepare all solutions.

2.2. Preparation of photocatalysts

Phosphorus doped porous ultrathin g-C$_3$N$_4$ nanosheets (PCN-S) were prepared according to the previous publication with some modifications [38]. In a typical synthesis, first of all, 2-aminoethylphosphonic acid (AEP) and melamine with a weight ratio of 1:60 were dissolved thoroughly in deionized water and heated to 80 °C, and kept stirring at 80 °C to evaporate the solvent completely. Then the remaining crystal complex was milled into powder and placed in a cover quartz container, and subsequently heated in a cube furnace under N$_2$ ambient from room temperature to 500 °C, and kept at this temperature for 3 h. Next the temperature was increased to 550 °C and continued to heat the sample for another 5 h. Finally the brown agglomerates were obtained and grounded into powder. The brown powder was labeled as PCN-B. To synthesize PCN-S, the thermal exfoliation process should be experienced. The above-obtained PCN-B was placed into an open crucible and heated at muffle furnace under static air from
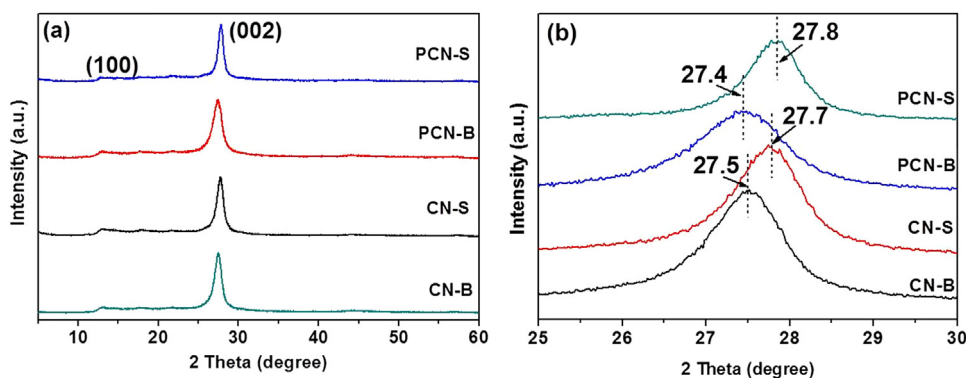
Fig 1. (a) XRD patterns and (b) the relative enlarged view of (002) peaks for the prepared CN-B, CN-S, PCN-B and PCN-S samples.
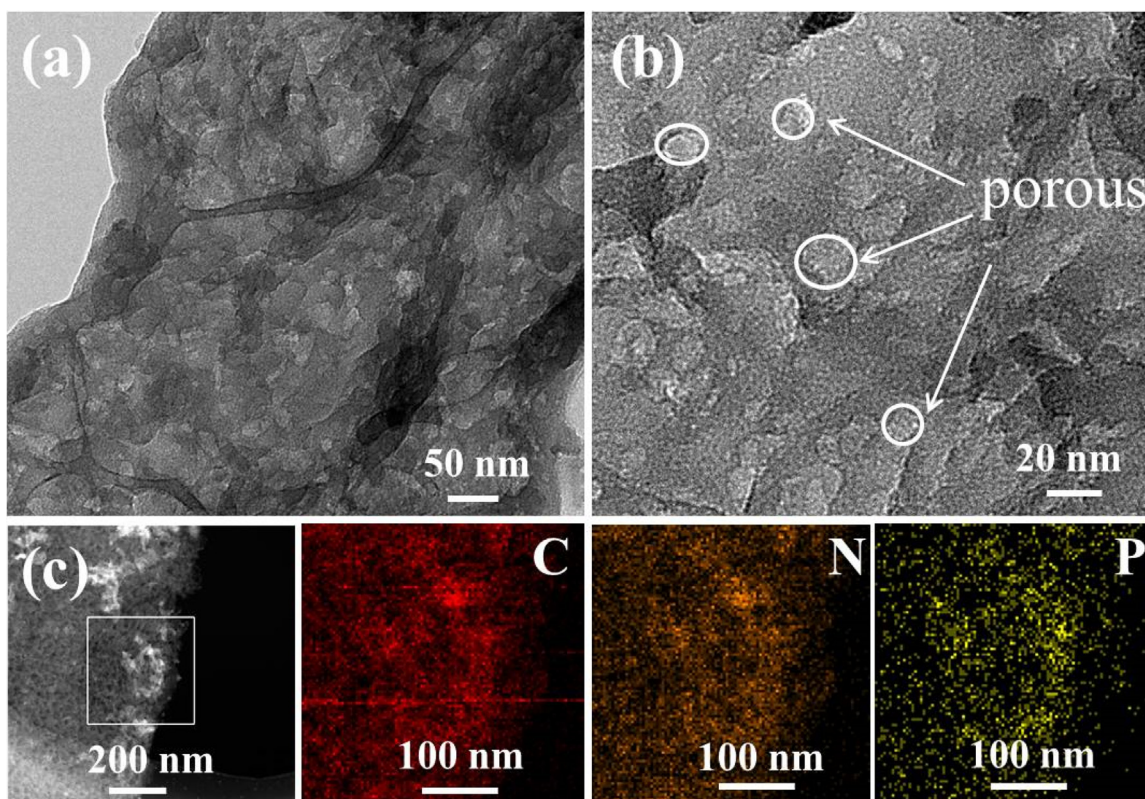

Fig. 2. (a) Low and (b) high resolution of TEM images of PCN-S, and (c) STEM of PCN-S and the corresponding EDS mapping of C, N and P elements.

room temperature to 500 °C, and kept at this temperature for 2 h. Then the obtained light-brown product was labeled as PCN-S. Bulk g-C$_3$N$_4$ (CN-B) was synthesized by the same method for the synthesis of PCN-B except that only melamine was placed to undergo the thermal polycondensation process. Then the CN-B was obtained by milling the yellow agglomerates into powder. The g-C$_3$N$_4$ nanosheets (CN-S) were obtained by further thermal exfoliating the above-obtained CN-B under the same condition like that for the preparation of PCN-S.

2.3. Characterizations

The crystal structure of the samples was studied by using an X-ray diffractometer (XRD) (Bruker AXS D8 Advances) at a scan rate (2θ) of 0.05° s^{-1} with Cu Kα irradiation source. To characterize the detailed morphology of the samples, field-emission scanning electron microscopy (FE-SEM) (Hitachi S-4800, Japan)

with an accelerating voltage of 5 kV and transmission electron microscopy (TEM) (JEOL JEM-3010) with an accelerating voltage of 200 kV were used. Atomic force microscopy (AFM, Nanoscope Mutimode IIIa, Veeco Instruments) measurement was conducted to evaluate the morphology of the obtained samples with Si-tip cantilever. FT-IR spectra were carried out on an IRAffinity-1 Fourier transform infrared spectrometer. Chemical compositions of the CN-B, fresh PCN-S and PCN-S after photocatalytic process were analyzed using X-ray photoelectron spectroscopy (XPS, ESCALAB 250Xi, Thermo Fisher). The specific surface areas of the samples were characterized via a nitrogen adsorption-desorption and Brunauer-Emmett-Teller (BET) method by a surface area analyzer (NOVA 2200e, Quantachrome). The photoluminescenece (PL) spectra were studied through F-7000 fluorescence spectrometer. Ultraviolet visible diffused reflectance spectra (UV-vis DRS) were used to study the optical property of the synthesized samples by a UV–vis spectrophotometer (Cary 300, USA) equipped with an inte-

grating sphere. The total organic carbon (TOC) assays were studied via a Shimadzu TOC-VCPH analyzer.

2.4. Evaluation of photocatalytic activity

The Cr(VI)/2,4-DCP mixed reaction solution was prepared by diluting certain volume of Cr(VI) and 2,4-DCP stock solution to 50 mL with deionized water in a quartz vessel. Unless otherwise mentioned, the concentration of Cr (VI) and 2,4-DCP in the mixed solution were 20 mg/L and 80 mg/L, respectively. A 300 W Xe lamp (PLS/SXE 300C, Beijing Perfectlight Co., Ltd.) equipped with a UV cut of filter ($\lambda > 400$ nm) was used as the visible light source. Before irradiation start, 50 mg photocatalysts was added to the reaction solution and kept stirred in dark for 1 h to reach the adsorption-desorption equilibrium. During the photoreaction process, 3 mL of aliquots were collected and sampled at certain time interval for subsequent analysis after centrifugation and filtration to remove the photocatalyst. The real time concentrations of Cr(VI) was determined colorimetrically using the diphenylcarbazide method at 540 nm with a UV-2550 UV–vis spectrophotometer according to our previous studies [52,53]. The concentration of 2,4-DCP was determined by HPLC (Agilent 1100). Before determination, the samples were filtered by 0.45 μm membrane, and then the filtrates were performed using HPLC with the UV detector at 280 nm. The HPLC was equipped with a Kromasil C18 column (250×4.6 mm) and worked at 25 °C. The mobile phase was 70:30 (v/v) acetonitrile (CH_3CN) and ultrapure water, and the flow rate was 1 mL min^{-1}. The compounds were identified by comparing retention times with standard samples and then quantified with calibration curve method [54].

To study the stability and regeneration ability of the prepared samples, cycling experiments were conducted. In cycling experiments, the photocatalysts was collected by centrifugation and washed thoroughly with ethanol and deionized in order to completely remove the residual materials. Subsequently, the recycled samples were added into fresh Cr (VI) and 2,4-DCP mixed aqueous solution ($K_2Cr_2O_7$: 20 mg/L, 2,4-DCP: 80 mg/L) to conduct another photocatalytic process.

2.5. Photoelectrochemical measurement

Photoelectrochemical tests were carried out on a CHI 660D workstation in a three-electrode model, utilizing a Pt electrode as the counter electrode and an Ag/AgCl electrode as the reference electrode. Typically, the working electrodes were prepared as follows: 10 mg of the photocatalyst was suspended in 1 mL 0.5% Nafion solution to make slurry. Then, 100 μL of the slurry dropped onto a 1 cm × 2 cm FTO slice with an effective working area of 1 cm^2. A 300 W Xe arc lamp served as a light source. The electrochemical impedance spectroscopy (EIS) was performed in 0.2 Na_2SO_4 aqueous solution based on the above three-electrode system.

3. Results and discussion

3.1. Crystal structure and morphology

The crystal structure properties of the prepared samples were evaluated by the X-ray diffraction (XRD) patterns. As shown in Fig. 1a, all the diffractograms present two main peaks of (002) and (100). The former one around 27° presents typical interlayer-stacking peal, and the latter one is around 13° indicating the in-plane structural motif or the heptazine units [45,55,56]. The two peaks are consistent with those of bulk g-C$_3$N$_4$ (JCPDS 50-1250). It should be noted that the PCN-S shows similar XRD patterns to CN-B, indicating that the original crystal structure of g-C$_3$N$_4$ is largely retained after the doping of the P element and the post thermal

Table 1
BET surface areas and pore volumes of the as-prepared samples.

Samples	S_{BET} (m^{2}g^{-1})	Pore volume (cm^{3}g^{-1})
CN-B	4.4	0.06
CN-S	91.5	0.46
PCN-B	13.7	0.07
PCN-S	102.5	0.53

exfoliation process. To evaluate the crystal structure changes of the prepared samples, it is necessary to further analyze the (002) peaks of XRD pattern. It is well-known that the diffraction peak (002) is a typical feature representing the interlayer stacking reflection of conjugated aromatic system. Just as shown in Fig. 1b, for CN-B, the peak center of (002) located at 27.5°, but for PCN-B, the peak center of (002) shift to 27.4°, which means that the interlayer distance is increased after the doing of P element, because of the larger radius of the doped P atom than that of the replaced C atom [57]. However, thermal exfoliation of CN-B leads to the shift of (002) peak from 27.5° to 27.7° for CN-S, and also leads to the shift of (002) peak from 27.4° to 27.8° for PCN-S, which could be due to the decrease of the interlayer distance after thermal heat treatment. This phenomenon could be attributed to the surface flattening process of the undulated single layers in PCN-B during the heat treatment, leading to the denser packing of layers in PCN-S, indicating the successful exfoliation of the layered PCN-B [58,59]. Therefore, the analysis mentioned above implies the successful doping of P element and the thermal exfoliation of bulk PCN-B to PCN-S.

The morphology of the prepared samples was investigated by SEM and the images were shown in Fig. S1. As seen clearly in Fig. S1a, CN-B forms solid agglomerates with a size of several micrometers. Different from CN-B, the CN-S appears as loose and nanosheets-liked soft agglomerates (Fig. S1b). As for PCN-B and PCN-S (Fig. S1c and S1d), the morphologies and changes are similar to those of CN-B and CN-S, respectively. AFM measurement was also conducted to demonstrate the nanosheet structure of the prepared samples (Fig. S2). The cross-sectional AFM image shows that the average thickness of PCN-S is about 3.32 nm, which could serve as a strong evidence for the existence of the nanosheet structure for the prepared PCN-S sample. To further investigate the detailed morphology of the prepared PCN-S, low and high-resolution TEM images of the prepared PCN-S were shown in Fig. 2a and b. It can be seen that the PCN-S presents nanosheet structure, which is already confirmed by the SEM images. Besides, the surface of the nanosheets is not smooth and there exist randomly distributed in-plane mesopores of several to tens of nanometers on the carbon nitride nanosheets. These well-defined and open-up surface pores existing on the PCN-S can provide quantities of active sites and improve mass transportation and photogenerated charge separation rate in nanodomains, which can further utilize the advantages of the π-conjugated system for photocatalytic employments. The EDS data of PCN-S shown in Fig. S3 confirmed the existence of C, N, and P element in the prepared PCN-S. To gain further intuitive characterization of the uniform distribution of the element, the energy dispersive X-ray spectroscopy (EDS) element mapping images of the prepared PCN-S was also provided(Fig. 2c). It can be seen that the elements of C, N, P are distributed uniformly throughout the whole structure of PCN-S at the nanoscale.

Nitrogen adsorption-desorption isotherms of all the samples were measured to further study the morphology and pore distribution. As shown in Fig. S4, the isotherms of all samples exhibit a classical type IV, indicating the presence of mesopores. Owing to the emission of ammonia gas during the thermal condensation process, some pores would be produced on the surface of PCN-S, which is in good agreement with TEM analysis. The BET surface areas and pore volume of the as-prepared samples were collected in Table 1.
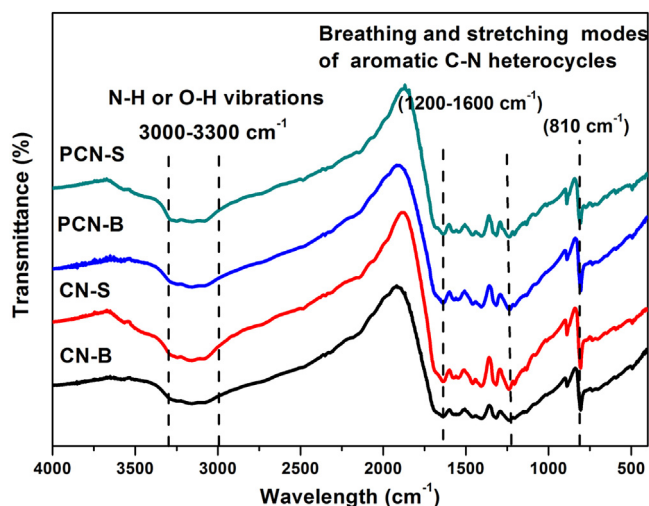
Fig. 3. FTIR spectra of CN-B, CN-S, PCN-B and PCN-S.

We can see that the specific surface area calculated from the linear part of the multipoint plot of PCN-S is 102.5 m^2/g^{-1}, which is larger than that of CN-S (91.5 m^2/g^{-1}), and much larger than those of CN-B (4.4 m^2/g^{-1}) and PCN-B (13.7 m^2/g^{-1}), further demonstrating the ultrathin structure of PCN-S. It is well known that the large surface area means that more active species and reactants can be absorbed on its surface. These data are consistent with the morphologies of the samples, which highlights the important role of the combination of element doping and thermal exfoliation method in creating such a distinctive texture of PCN-S. The results mentioned above further demonstrate the successful preparation of PCN-S which possesses nanosheet structure with in-plane pores on the surface.

3.2. Chemical group and chemical states

The FT-IR analysis of all the samples was performed to reveal the structure variation after the doping of P element and the thermal treatment. As depicted in Fig. 3, with respect to g-C$_3$N$_4$, a series of peaks in the region of 1200–1600 cm^{-1} can be related to the typical stretching modes of CN heterocycles, wherein the peak located at 810 cm^{-1} is assigned to the bending vibration of heptazine rings, indicating the major structure of g-C$_3$N$_4$ was retained after the doing of P element and the further thermal condensation process. The retained g-C$_3$N$_4$ structure of PCN-S is essential for π-delocalized electronic systems to generate and transfer photogenerated charges for the redox reaction process in the photocatalytic system. The broad absorption band located at around 3000–3300 cm^{-1} can be attributed to the stretching vibration of N—H or O—H bond, originated from the uncondensed amino groups [45,55,56]. It should be noted that due to the relatively low concentration of P element and the overlap effect of these strong C—N vibrations, the vibration band referring to P-related functional groups can hardly be observed.

X-ray photoelectron spectra (XPS) were also conducted to study the chemical compositions of the obtained materials, and the results were shown in Fig. 4. It can be found the g-C$_3$N$_4$ is mainly composed of C, N and O elements, and P element cannot be observed in the survey spectrum due to the relative low concentration. The C 1s spectrum of g-C$_3$N$_4$ can be divided into two main peaks located at 284.54 eV and 287.84 eV, respectively. The peak at 284.54 eV can be attributed to the C=C—C bonds. The main peak with a binding energy of 287.84 eV can be identified as a sp^2-hybridized carbon in an N-containing aromatic ring (N—C=N). There is an extra peak located at 286.03 eV in the C 1s spectrum, which is attributed to the C-N. As for N 1s spectrum, it can be separated into three peaks

with the binding energy at 398.29 eV, 400.20 eV, and 404.04 eV, respectively. The major peak located at 398.29 eV is assigned to sp^2-hybridized nitrogen in C-containing triazine rings (C—N=C). The peak at 400.20 eV indicates the tertiary nitrogen (N–(C)$_3$), and the peak at 404.04 eV is attributed to charging effects of positive charge location. [59] The XPS analysis of C 1s and N 1s further confirms the existence of triazine heterocyclic ring structure in the P-doped g-C$_3$N$_4$. As for P 2p spectrum, in CN-B spectrum, there is no P 2p peak, indicating a negligible content of P element. However, in PCN-S, the P 2p signal can be separated into three peaks located at about 133.04 eV, 133.79 eV and 134.95 eV, respectively. The peaks at 133.04 eV and 133.79 eV are contributed to the P-N species, which indicates the replacement of C atoms by the P atoms in the C-N framework of g-C$_3$N$_4$ during the doping of P elements process. Besides, it is reported that the energy of P-N is lower than that of P=N. So, the peaks at 133.04 and 133.79 eV refer to the P-N and P=N bonds, respectively. In addition, the peak at 134.95 eV can be attributed to the P=O bond, which was produced owing to the reaction between P element and O$_2$ during the thermal condensation process in air at high temperature [38,47]. The XPS analysis is also a proof to confirm the successful doping of P element in the PCN-S. And meanwhile, to more clearly investigate and compare the changes of the PCN-S after the photocatalytic reaction, the XPS spectra of the used PCN-S photocatalyst was also provided. It is clear to see that the main peaks of the used PCN-S were kept similar to fresh PCN-S, and no obvious changes can be observed about the C 1s, N 1s and P 2p spectrum, which means the high stability of the prepared PCN-S.

3.3. Optical properties and electronic band structure

The optical properties of the prepared samples were studied by the UV–vis diffuse reflectance spectra, and the results were shown in Fig. 5a. It is clear to see that the absorption edge of CN-B is limited under 450 nm, but after the doping of P element, the adsorption edge of PCN-B is broaden to the whole visible-light region (400 nm < λ < 800 nm), which accounts for 53% of the whole solar spectrum. And it should be noticed that the thermal condensation process narrows the absorption edge of the samples in some extent, indicating the change of the band gap of the prepared samples, so the band gap of all the samples were acquired by the Kubelk-Munk method:

$$(\alpha h\nu)^n = A(h\nu - Eg), \tag{1}$$

where α is the absorption coefficient, $h\nu$ is the light energy, A is a constant, Eg is the optical band gap energy and n is equal to 2 for g-C$_3$N$_4$ based materials [38,60]. The obtained results were shown in Fig. 5b and 5c. In fact, the band gap of the prepared samples experienced different changes during the P element doping and thermal exfoliation process. After the doping of P element, the band gap of CN-B is narrowed from 2.74 eV to 2.69 eV for PCN-B. However, the subsequent thermal exfoliation enlarges the band of PCN-B from 2.69 eV to 2.92 eV for PCN-S, owing to the aroused effect of QCE due to the formation of the ultrathin nanosheet structure [55,61]. Moreover, according to the common equations, the valence band (E$_{VB}$) and conduction band (E$_{CB}$) edge position of the as-prepared samples were obtained and shown in Table 2 [41,62].

$$E_{CB} = X - E_C - 1/2 Eg \tag{2}$$

$$E_{VB} = E_{CB} + Eg \tag{3}$$

where E$_C$ is the energy of free electrons on the hydrogen scale (about 4.5 eV), X is the electronegativity of the semiconductor, and the values of the X for g-C$_3$N$_4$ is 4.72 eV. According to the data shown in Table 2, the E$_{CB}$ of PCN-S is −1.24 eV, which is more negative than that of the CN-B, CN-S and PCN-B, and the E$_{VB}$ of the PCN-S
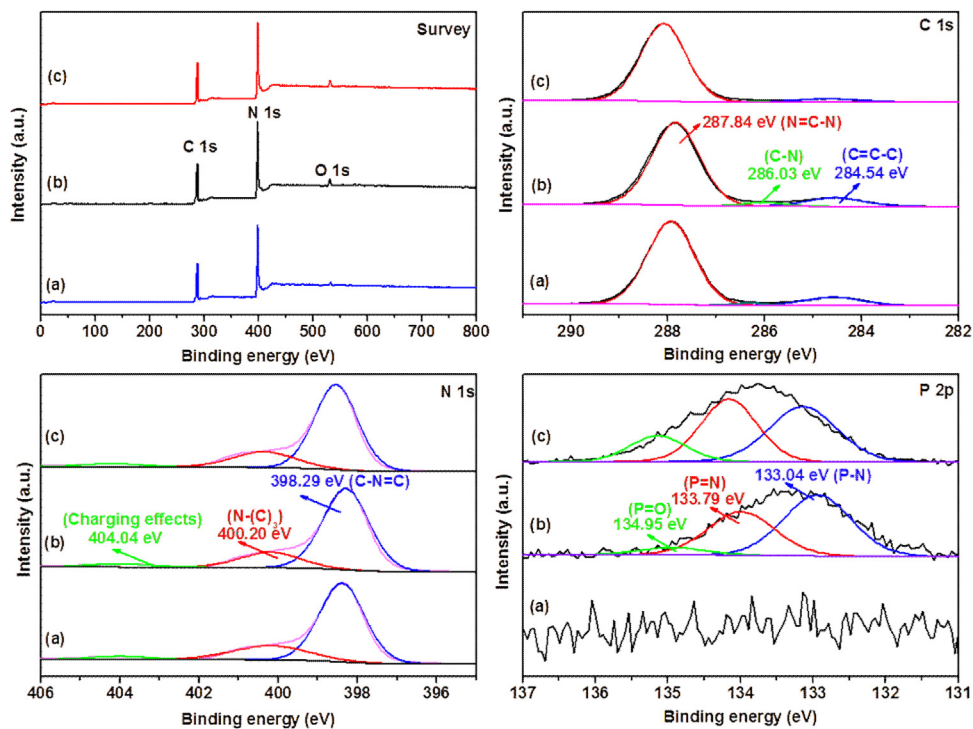
Fig. 4. The XPS spectra of (a) CN-B, (b) PCN-S (b) and (c) PCN-S photocatalyst after photocatalytic reaction.
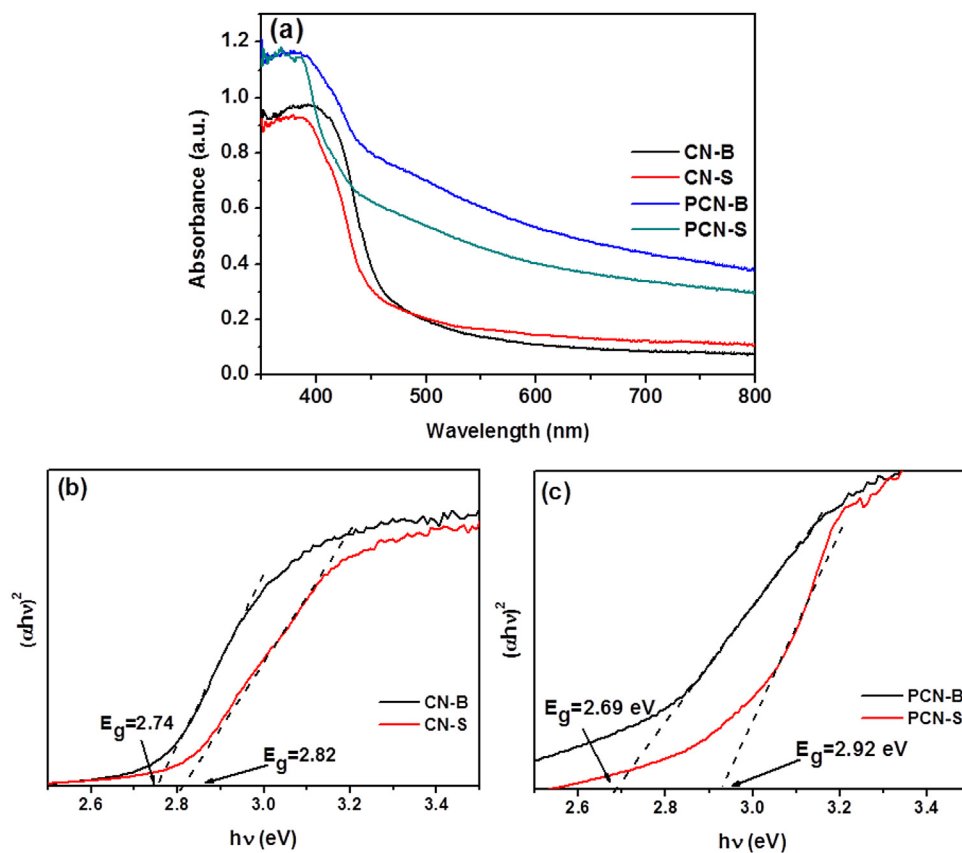

Fig. 5. (a) UV–vis diffuse reflectance spectra of CN-B, CN-S, PCN-B and PCN-S, (b) the band gap energy of CN-B and CN-S, and (c) band gap energy of PCN-B and PCN-S.

is 1.68 eV, which is more positive than that of the other three samples. The result means that the prepared PCN-S presents enhanced redox ability.

In addition, previous studies have presented that the prepared g-C$_3$N$_4$ nanosheets by the exfoliation of bulk g-C$_3$N$_4$ can bring enhanced photocatalytic performance, but the consequent

Table 2
Band gap (E_g), relative conduction band (E_{CB}) and valence band (E_{VB}) of the as-prepared samples.

Samples	E_g (eV)	E_{CB}	E_{VB}
CN-B	2.74	−1.15	1.59
CN-S	2.82	−1.19	1.63
PCN-B	2.69	−1.13	1.56
PCN-S	2.92	−1.24	1.68
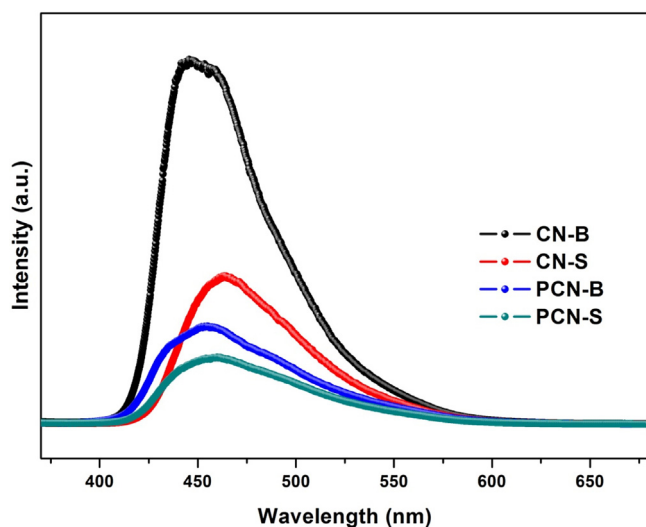
Fig. 6. Photoluminescence spectra of the prepared samples.

Fig. 7. (a) Photocurrent response and (b) EIS Nyquist plots of the prepared samples.

increased band gap severely limits the photocatalytic performance of the prepared g-C$_3$N$_4$ nanosheets. However, different from previous reports, the prepared PCN-S in this study presents a very strong tail absorption (Urbach tail) in the visible-light region. In most cases, the appearance of Urbach tail means the existence of mid-gap states [38,63]. Thus, the existed empty mid-gap states can adapt the photogenerated electrons generated from the valence band (VB) of PCN-S, which can promote the adsorption of the photons smaller than the band gap, leading to the existence of the Urbach tail. Thus it can be seen that after the doping of P element, both PCN-B and PCN-S produce Urbach tail in their UV–vis diffuse reflectance spectra, but no Urbach tail can be observed for the CN-B and CN-B, indicating that the appearance of mid-gap states is attributed to the P doping, instead of thermal exfoliation process.

3.4. Photogenerated electron-holes separation and transport

To study the generation and separation of the photogenerated electron-holes pairs of the prepared samples, the photoluminescence (PL) emission spectroscopy was provided. As shown in Fig. 6, the CN-B shows the highest PL peak intensity, which means the high recombination efficiency between the photogenerated electrons and holes. However, after the P doping, the formed PCN-B presents a much lower PL peak intensity than CN-B, indicating the inhibited photogenerated charge recombination efficiency, owing to the increased charge diffusion rate and charge mobility of PCN-B. Additionally, the lower charge recombination efficiency of PCN-B than CN-B also demonstrated that the existing of P element doesn't act as a recombination center for the photogenerated electrons and holes. On the other hand, CN-S also shows lower PL peak intensity than that of CN-B, indicating that the formation of ultrathin nanosheets can increase the photogenerated electron-holes separation efficiency. In addition, the enlarged band gap due to the strong QCE can also promote the transportation and separation of the photogenerated charges. The most important thing to be
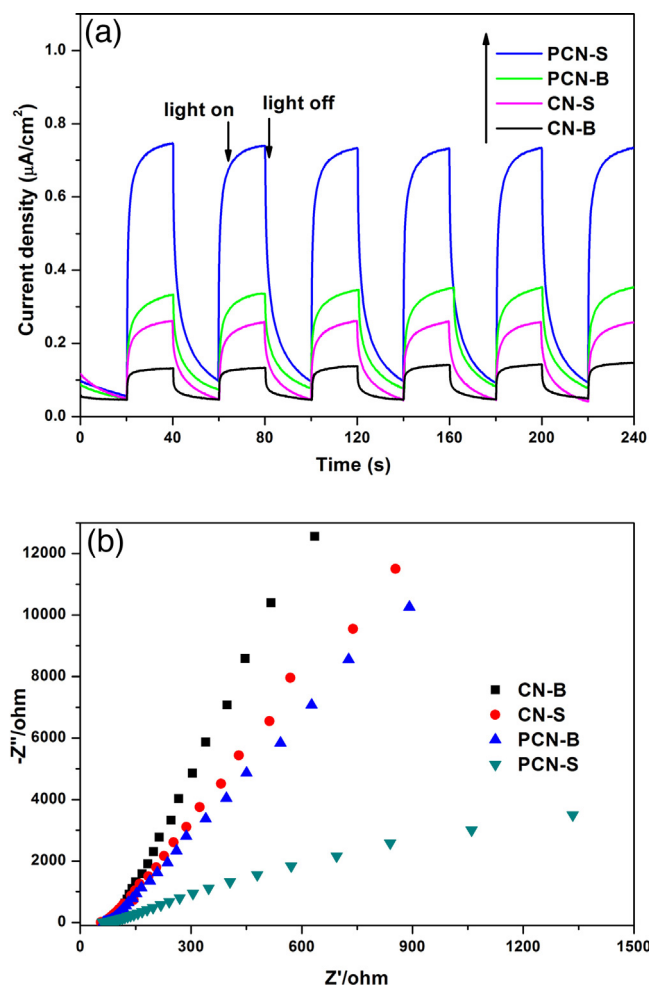
noticed is that the PCN-S presents the smallest PL peak intensity, implying lowest photogenerated charges recombination efficiency. This result confirmed that the thermal exfoliation process does not destroy the electronic structure of the P-doped aromatic system, which can strictly inhibit the charge separation and transportation. In fact, the combination of the P doping and thermal exfoliation process for the formation of PCN-S can merge the advantages, thus presenting a low recombination efficiency of the photogenerated electron-holes and high photocatalytic activity.

The transient photocurrent measurement is an efficient way for the comprehensive study of the photo-response ability and photogenerated charges recombination efficiency of the photocatalyst. As shown in Fig. 7a, it is clear to see that all the electrodes present rapid and stable photocurrent response, and the photoresponsive phenomenon is entirely reversible upon each light irradiation. However, different samples present different light response ability. Among all the samples, the PCN-S present the highest photocurrent density, and much higher than that of CN-B, CN-S and PCN-B, implying the higher light harvesting and low photogenerated charges recombination efficiency. EIS is an efficient electrochemical method to explain the electron-transfer efficiency at the electrodes [47]. Fig. 7b discloses the semicircular Nyquist plots for all the samples, and CN-B shows the biggest diameter, implying the poor electrical conductivity inhibiting the electron transfer from carbon nitride to the back-contact electrode. In comparison, PCN-S presents the smallest diameter, indicating the lowest charge trans-

fer impedance, owing to the doping of P element and the formation of porous nanosheet structure.

3.5. Effect of P element doping and thermal exfoliation for the photocatalytic activity

The photocatalytic activity of the prepared samples was first evaluated by the photocatalytic reduction of Cr(VI), and the results was shown in Fig. S5a. It is clear to see that CN-S presented higher performance than that of CN-B, which indicated that thermal exfoliation process can increase the specific surface area greatly, so the reaction sites could increase, and the transfer length of the photo-generated charges would decrease due to the production of g-C$_3$N$_4$ nanosheets. And meanwhile, we can see that the PCN-B also exhibited a higher photocatalytic activity than that of CN-B, and equal to that of CN-S, which indicated the P doping can increase the utilization efficiency of visible light and promote the photogenerated electron-hole transportation efficiency. Obviously, among all the prepared samples, PCN-S exhibits the highest activity of Cr(VI) reduction under visible light illumination. Meanwhile, the adsorption abilities of the prepared samples towards Cr(VI) were also investigated to estimate their effect for the photocatalytic performance. As shown in Fig. S5b, it can be seen that PCN-S presents the highest adsorption capacity than the other three samples, and their adsorption abilities follow the order: PCN-S > CN-S > PCN-B > CN-B. It should be noted that though the adsorption capacity of CN-S was higher than PCN-B, their photocatalytic ability for Cr(VI) was nearly equal. The results indicated that combination of P doping and thermal exfoliation can greatly promote the photocatalytic performance of g-C$_3$N$_4$, and the final performance was the synergistic effect of the adsorption ability and photocatalytic ability, so PCN-S was chosen as the photocatalysts in the following experiments.

3.6. Synergistic photocatalysis of Cr(VI) reduction and 2,4-DCP degradation over PCN-S

The feasibility of the simultaneous photocatalysis of the Cr(VI) reduction and the 2,4-DCP oxidation over PCN-S was firstly conducted in a mixed solution that containing Cr(VI) and 2,4-DCP. As shown in Fig. 8a and b, 20 mg/L Cr(VI) was nearly completely reduced over PCN-S after 120 min under visible light irradiation. And meanwhile, in the mixed reaction system, 80 mg/L 2,4-DCP was also degraded after 120 min irradiation. The result indicated that the simultaneous photocatalysis reduction of Cr(VI) and oxidation of 2,4-DCP were achieved successfully. In addition, some control experiments were conducted to analyze the role of each substrate in this reaction system. Just as shown in Fig. 8a, in the absence of PCN-S, the reduction efficiency of Cr(VI) in a mixed Cr(VI)/2,4-DCP under visible light irradiation is very low and nearly can be neglected. And the photocatalytic activity of PCN-S in a single Cr(VI) solution was also relatively low. Some researchers also reported the similar low reaction efficiency between Cr(VI) and chlorophenol under visible light irradiation [64,65]. It is well known that PCN-S can produce photogenerated electrons and holes under visible light irradiation, then the photogenerated electrons can migrate and work with Cr(VI) for it reduction process. However, though the photo-response ability and specific surface area of the prepared PCN-S is promoted when compared with pristine bulk g-C$_3$N$_4$, it is still difficult to achieve very high separation efficiency of photogenerated electron-holes and then work for the reduction of Cr(VI) in the absence of electron donor, 2,4-DCP. As for 2,4-DCP, only approximately 10% decrease was achieved within 120 min in the 2,4-DCP/Cr(VI) mixed system, which is similar to the low reduction efficiency of Cr(VI) in Fig. 8a. Once the PCN-S was added into the single solution of 2,4-DCP, its photocatalytic degradation increased greatly, but it still cost 120 min to complete removal of
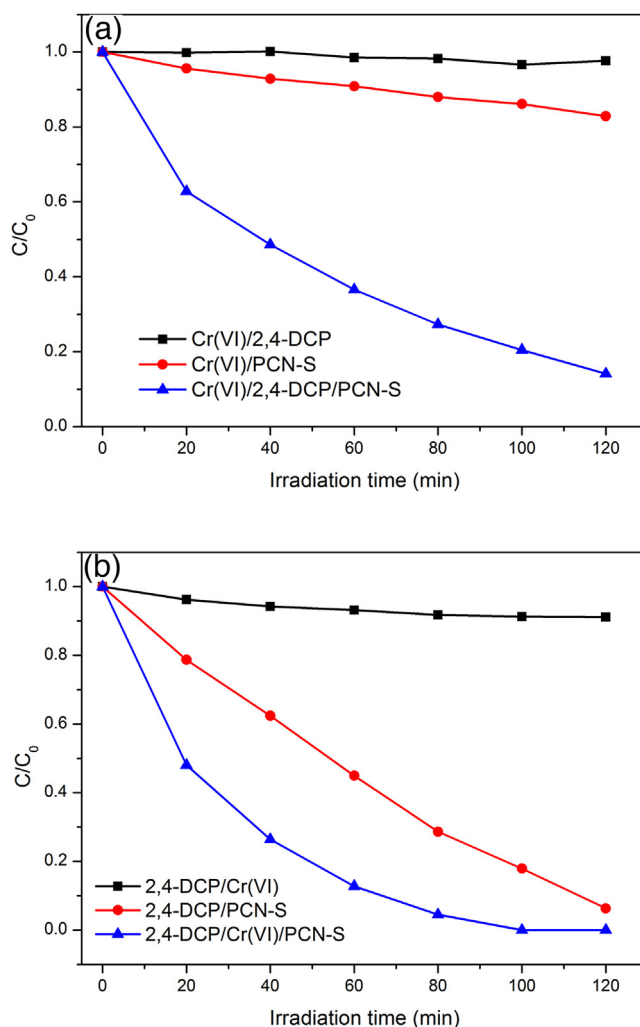

Fig. 8. The synergistic effect of Cr(VI) reduction and 2,4-DCP degradation over PCN-S under visible light irradiation: (a) Cr(VI) reduction and (b) 2,4-DCP degradation.

2,4-DCP. However, in the 2,4-DCP/Cr(VI)/PCN-S system, 2,4-DCP can be removed completely within 80 min. Under the same reaction condition, the total organic carbon (TOC) removal efficiency of 2,4-DCP in the reaction system was also investigated. [66–68]. As shown in Fig. S6, after two hours' visible light irradiation, 70.32% of the TOC was removed, which means that this synergistic reaction system not only presents high photodegradation efficiency of 2,4-DCP, but also shows relative high mineralization ability. These results demonstrated the existence of synergistic effect during the photocatalytic reduction of Cr(VI) and oxidation of 2,4-DCP.

3.7. Effects of substrate concentrations and the pH value

According to the results mentioned above, 2,4-DCP and Cr(VI) improved each other's removal efficiency in the PCN-S photocatalytic reaction system. So, various Cr(VI)/2,4-DCP mixed solution were applied to study the effect of the initial concentration of 2,4-DCP and Cr(VI). Fig. 9a shows that low concentration (10 mg/L) of 2,4-DCP cannot efficiently consume the holes, so the photocatalytic reduction efficiency of Cr(VI) was still low. Then with the concentration of 2,4-DCP increase, the photocatalytic reduction of Cr(VI) was also increased, and the reduction of Cr(VI) reached the maximum when the concentration of 2,4-DCP is 80 mg/L. After that, further increasing the concentration of 2,4-DCP to 100 mg/L, its photocatalytic activity decreased. Fig. 9b shows that 2,4-DCP degra-
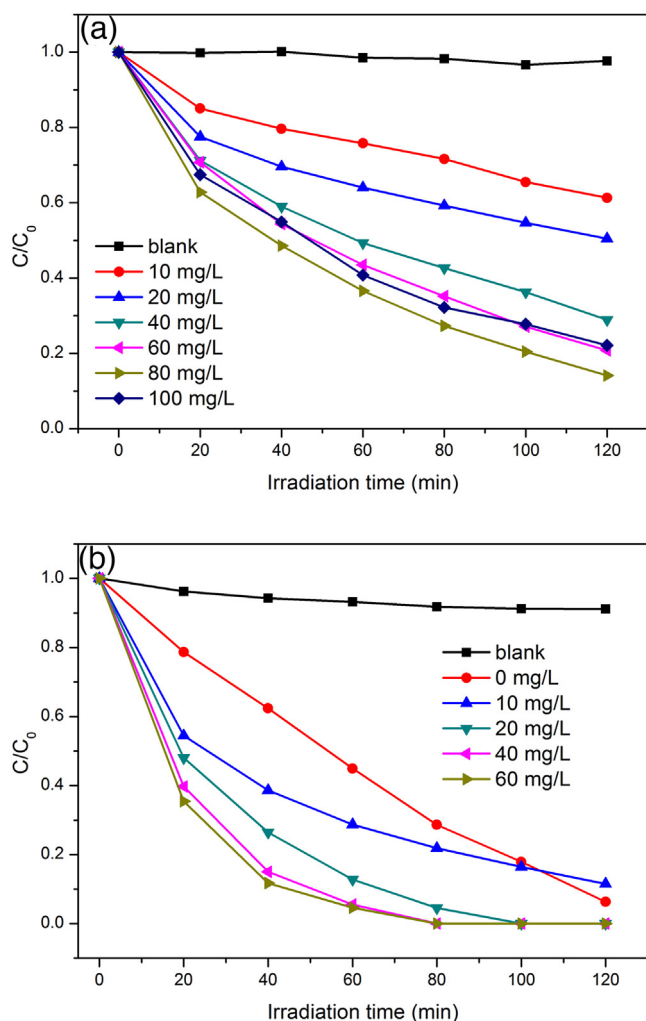
Fig. 9. The effects of (a) 2,4-DCP initial concentration on Cr(VI) (20 mg/L) reduction and (b) initial concentration on 2,4-DCP (80 mg/L) degradation.

Fig. 10. (a) Cr(VI) reduction and (b) 2,4-DCP degradation at different pH condition in the 2,4-DCP/Cr(VI)/PCN-S reaction systems.

dation rates increased along with the initial concentration of Cr(VI) increasing from 0 to 40 mg/L. And meanwhile, no obvious increase of 2,4-DCP degradation rate happened with further increasing the concentration of Cr(VI) to 60 mg/L. This phenomenon was caused by the fact that the active sites of the photocatalyst (PCN-S) were limited, when all the active sites were occupied and extra reactants could not work on the PCN-S surface, so the photocatalytic activity would not improve anymore. Thus taking the realistic application into account, 20 mg/L Cr(VI) and 80 mg/L 2,4-DCP were used in the following experiments.

Besides, to study the influence of pH value on the Cr(VI) reduction and 2,4-DCP oxidation, a series of experiments under different pH values were conducted, and the results are shown in Fig. 10. Obviously, both Cr(VI) reduction and 2,4-DCP oxidation rates experience a rapid increase by the decreasing of the pH values, especially for the Cr(VI) reduction. However, under alkaline condition, the Cr(VI) reduction and the 2,4-DCP oxidation were very low. The reasons for the sensitivity of the Cr(VI) reduction over different pH values of the reaction solution can be explained as follows: (1) at low pH, $HCrO_4^-$ or $Cr_2O_7^{2-}$ was the major Cr(VI) species, and the photocatalytic Cr(VI) reduction happens according to Eq. (4); (2) for alkaline medium, CrO_4^{2-} was the predominant specie, and the reaction process can be described by Eq.(5). The increasing reduction rate of Cr(VI) along with the increasing acidity can be explained owing to the higher sensitivity of $HCrO_4^-$ or $Cr_2O_7^{2-}$ than CrO_4^{2-}
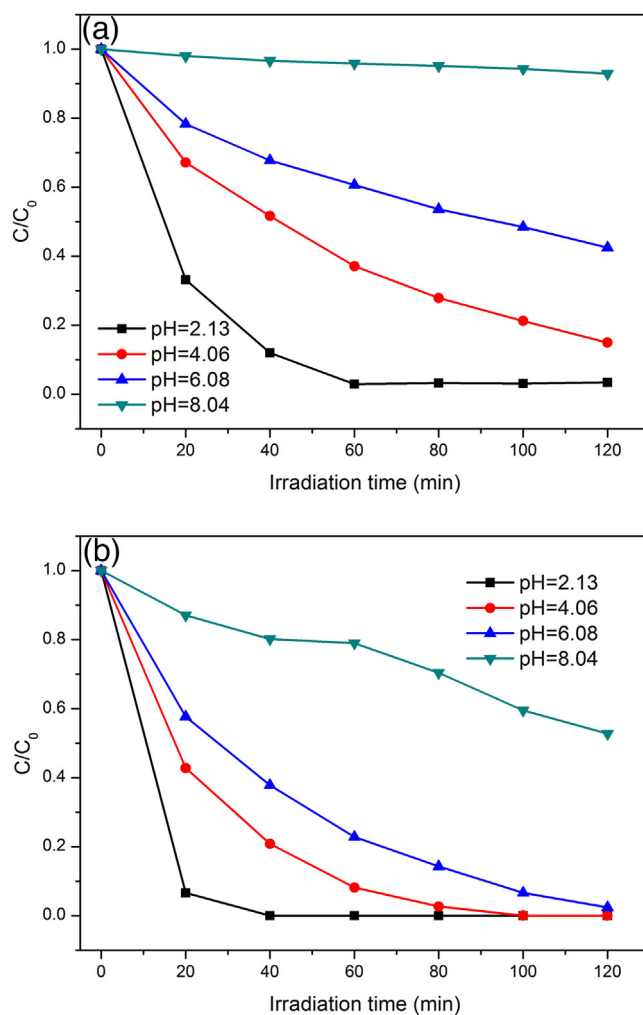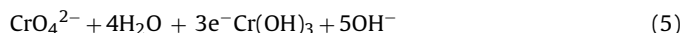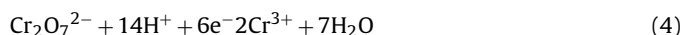
to experience the reduction process. But in the neutral and alkaline conditions, Cr(III) tend to precipitate on the surface of PCN-S for the formation of $Cr(OH)_3$, inhibiting the photocatalytic activity of the photocatalyst.

$$Cr_2O_7^{2-} + 14H^+ + 6e^- 2Cr^{3+} + 7H_2O \qquad (4)$$

$$CrO_4^{2-} + 4H_2O + 3e^- Cr(OH)_3 + 5OH^- \qquad (5)$$

To further demonstrate the existence of Cr(III) or the $Cr(OH)_3$ on the surface of PCN-S, the XPS analysis of Cr 2p for the used PCN-S under neutral condition was provided (Fig. S7). The peaks located at 577.44 eV and 587.69 eV can be attributed to the Cr(III) and Cr(VI), respectively. The introduction of Cr(III) on the surface of the used PCN-S under neutral condition means the formation of $Cr(OH)_3$, due to the fact that the $Cr(OH)_3$ appeared at the pH value of 4, and when the pH value reached 6.8, nearly all of the Cr(III) existed as the form of $Cr(OH)_3$ precipitation.

3.8. Effects of N_2 or air ambient and different sacrificial agents

The oxygen dissolved in the reaction solution can help the generation of numerous oxidizing species, and improve the oxidation reaction and suppress the reduction activity. As for the reaction under N_2 ambient condition, before the experiments was began, the reaction solution was purged by high purity N_2 (> 99.999%) for 1 h to remove the dissolved O_2 as much as possible, and kept purging N_2
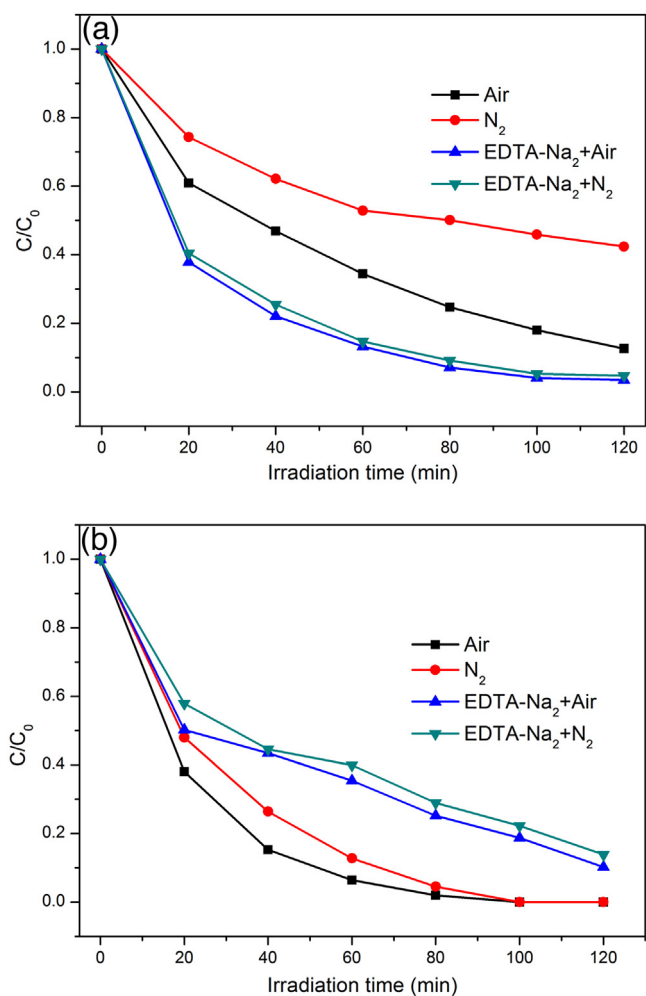
Fig. 11. (a) Cr(VI) reduction and (b) 2,4-DCP degradation with different scavengers and different ambient conditions under visible light irradiation in the Cr(VI)/2,4-DCP reaction system.
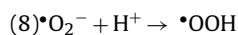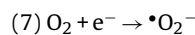
through the photocatalytic process. As shown in Fig. 11, both of the Cr(VI) reduction and 2,4-DCP oxidation rates in the mixed reaction system were higher in air ambient than those in N_2 ambient. The results demonstrated that O_2 played an important role in the photocatalytic reaction process. Under the condition of inflation, the dissolved O_2 can react directly with the photogenerated electrons to produce superoxide radical $\cdot O_2^-/\cdot OOH$ [65,69]. Superoxide radical can be further reduced to H_2O_2 or disproportioned to $\cdot OH$, these products are important for the degradation of organic pollutants in the photocatalytic reaction system. Besides, it has been reported that $\cdot O_2^-$ can reduce Cr(VI) to Cr(V). So in this study, $\cdot O_2^-$ may also tend to reduce Cr(VI) to its reduced products during the photocatalytic reaction process. Therefore, the rates of Cr(VI) reduction and 2,4-DCP oxidation are higher in air atmosphere than that in N_2 ambient.

Furthermore, we also studied the effects of the addition of EDTA-Na_2 on the photocatalytic reduction of Cr(VI) and oxidation of 2,4-DCP in Cr(VI)/2,4-DCP mixed solution. As shown in Fig. 11a, the photocatalytic activity of Cr(VI) of reduction obviously increases with the addition of 1 mM EDTA-Na_2. Since EDTA-Na_2 can serve as hole scavenger, which can promote the separation of photogenerated electron-holes and exhibits the promoting effect for the reduction of Cr(VI). Besides, when the reaction process was conducted under the N_2 atmosphere, the Cr(VI) reduction activity with EDTA-Na_2 experienced a slight decrease, attributing to the decreased electron transportation of the $O_2/\cdot O_2^-$ mediated reduc-

tion in the absence of dissolved oxygen. The results indicated that an efficient consumption of photogenerated holes can improve the photocatalytic reduction of Cr(VI) process. Fig. 11b shows the results of the photocatalytic activity of 2,4-DCP with the addition of EDTA-Na_2. It is clear to see that when EDTA-Na_2 was added into the mixed reaction system, the 2,4-DCP degradation efficiency decrease. This results can be explained as that EDTA-Na_2 also acts as hole scavenger, which will consume the oxidize species and compete with 2,4-DCP, and clearly implies that the 2,4-DCP degradation mainly depended on the photogenerated holes. And meanwhile, it also can be found that the photocatalytic efficiency for the degradation of 2,4-DCP in air is higher than that in N_2 ambient, due to the fact that the dissolved oxygen promotes the active oxidation of 2,4-DCP. But the effect of the dissolved oxygen was not so obvious in the presence of EDTA–Na_2, probably because the photocatalytic reaction rate was determined by the separation rate of the photogenerated electron-hole pairs in some extent, while the existence of EDTA-Na_2 could greatly consume the photogenerated holes, and promote the separation efficiency of the photogenerated electrons and holes. So the effect of dissolved oxygen in this reaction system was relatively weakened. In short, the synergistic photocatalytic reduction of Cr(VI) and oxidation of 2,4-DCP could rapidly consume photogenerated electrons-holes and generated active oxidation radicals in the mixed reaction solution, proving the enhanced photocatalytic activity of PCN-S.

3.9. Possible photocatalytic mechanism

Based on the experiment results, we proposed a probable mechanism for the photocatalytic reduction of Cr(VI) and oxidation of 2,4-DCP over PCN-S. PCN-S possesses porous ultrathin nanosheet structure, which means higher specific surface area and numerous active sites for the reaction process. The doping of P can broaden the visible light response region of the photocatalyst, which can promote the solar energy utilization efficiency. In this photocatalytic reaction system, Cr(VI) acts as an electron acceptor, which can react with the photogenerated CB electrons; and meanwhile, 2,4-DCP serves as an electron donor, which can react with the photoexcited holes. These two processes can promote the separation rate of photogenerated electron-holes, which results in much more CB electrons for Cr(VI) reduction and VB holes for 2,4-DCP oxidation. Under visible light irradiation, the PCN-S could generate electrons and holes. Subsequently, the photogenerated electrons in the conductor band of PCN-S could react with the dissolved oxygen to produce $\cdot O_2^-$ and migrate to Cr(VI) to form its reduced state of chromium. Meanwhile, the photogenerated holes left behind in the valence band of PCN-S could react with H_2O to produce $\cdot OH$. Then the reaction between $\cdot OH$ and H^+ could generate H_2O_2. Besides, $\cdot O_2^-$ not only works to 2,4-DCP, but also plays positive effect for the reduction of Cr(VI) via two-step $\cdot O_2^-$ mediated indirect reduction. However, due to the strong oxidation ability of H_2O_2, its existence would inevitably oxidize the reduced chromium back to Cr(VI). In addition, 2,4-DCP could be oxidized by the photogenerated holes and the produced oxidized species, such as $\cdot OH$, $\cdot O_2^-$ and H_2O_2. According to the analysis mentioned above, the generation of the photogenerated electron-holes, radicals and reaction process can be list as following equations:
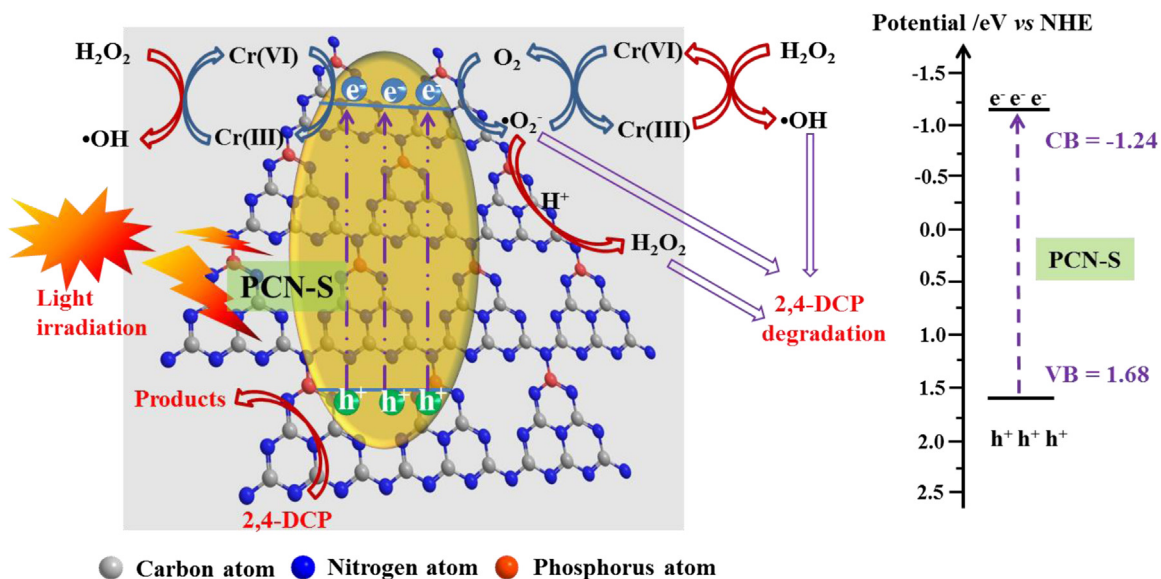
$$PCN\text{-}S + h\nu \rightarrow PCN\text{-}S(h^+ + e^-) \tag{6}$$

$$(7)\ O_2 + e^- \rightarrow \cdot O_2^-$$

$$(8)\cdot O_2^- + H^+ \rightarrow \cdot OOH$$

$$2\cdot O_2^- + 2H^+ \rightarrow O_2 + H_2O_2 \tag{9}$$

$$\cdot O_2^- + e^- + 2H^+ \rightarrow H_2O_2 \tag{10}$$

Fig. 12. A schematic illustration of simultaneous reduction of Cr(VI) and degradation of 2,4-DCP over PCN-S under visible light irradiation.
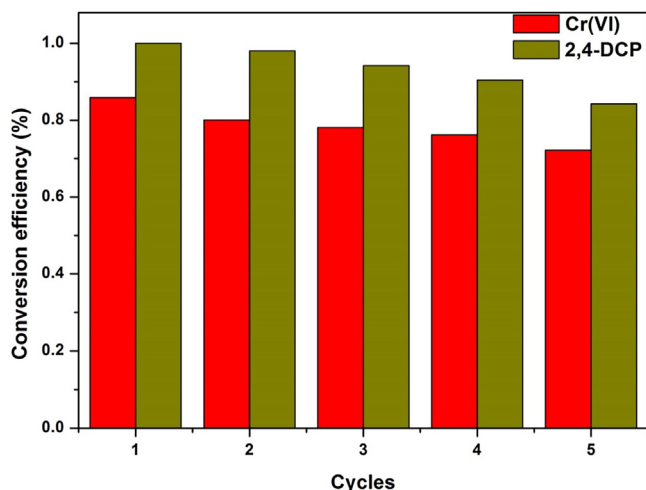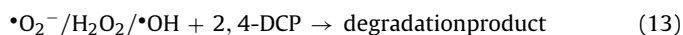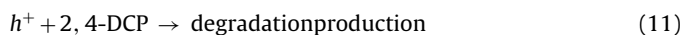

Fig. 13. The reusability of the PCN-S for the reduction of Cr(VI) and degradation of 2,4-DCP in the Cr(VI)/2,4-DCP reaction system.

$$H_2O_2 + e^- \rightarrow {}^\bullet OH + OH^- \tag{11}$$

$$h^+ + 2,4\text{-DCP} \rightarrow degradation production \tag{11}$$

$${}^\bullet O_2{}^- / H_2O_2 / {}^\bullet OH + 2,4\text{-DCP} \rightarrow degradation product \tag{13}$$

The overall reaction mechanism and process of Cr(VI) reduction and 2,4-DCP oxidation over PCN-S under visible light irradiation were shown in Fig. 12.

3.10. Repeatability and stability of photocatalysts

Considering the actual application of photocatalyst, the repeatability and stability of the photocatalyst are very important. So the photocatalytic repeatability of the PCN-S was studied by recycling experiment, and the results were shown in Fig. 13. It can be seen that even after 5 photocatalytic cycles, the photocatalytic efficiency for the Cr(VI) and 2,4-DCP oxidation can reach 75% and 90%, respectively, and no significant loss of the photocatalytic activity can be observed in cycling experiment. To further demonstrate the stability of the PCN-S, the XRD and FTIR of the fresh and used photocatalyst have been provided for comparison (Fig. S8a and S8b).

The results reveal that no significant changes happened in the crystal structure and surface chemical compositions of the photocatalyst after the photocatalytic reaction process. These results coupled with the XPS analysis in Fig. 4 indicated that PCN-S catalyst presents excellent recycling ability in the simultaneous photocatalytic reduction of Cr(VI) and oxidation of 2,4-DCP.

4. Conclusion

Phosphorus doped pores ultrathin g-C_3N_4 nanosheets (PCN-S) were successful synthesized via the combination of P doping and thermal exfoliation process. The prepared PCN-S owns porous structure, high specific surface areas and broadened visible light response region, and presents higher photocatalytic activity than as prepared CN-B, CN-S and PCN-B in the single Cr(VI) solution. In the mixed Cr(VI)/2,4-DCP reaction solution, PCN-S presents enhance photocatalytic activity for simultaneous photocatalytic reduction of Cr(VI) and oxidation of 2,4-DCP. Various reaction conditions were investigated to optimize the synergistic effect and study the detailed reaction mechanism. The results indicated that the initial concentrations of the Cr(VI) and 2,4-DCP will influence the photocatalytic degradation efficiency in a certain concentration range. Besides, we found that acidic environment and the existence of oxygen could promote the reduction of Cr(VI) and 2,4-DCP oxidation. Cycling experiments revealed that the prepared PCN-S presents high repeatability and stability. The detailed reaction mechanism over PCN-S for the photocatalytic reduction of Cr(VI) and oxidation of 2,4-DCP was proposed. It is expected that our study can provide new insight into the strategies for the design and utilization of efficient non-metal photocatalyst for environmental employment.

Appendix A. Supplementary data

Supplementary data associated with this article can be found, in the online version, at http://dx.doi.org/10.1016/j.apcatb.2016.10.046.

References

[1] P. Fu, P. Zhang, Appl. Catal. B-Environ. 96 (2010) 176–184.
[2] H. Fu, S. Zhang, T. Xu, Y. Zhu, J. Chen Environ. Sci. Technol. 42 (2008) 2085–2091.
[3] D.S. Wang, J. Zhang, Q.Z. Luo, X.Y. Li, Y.D. Duan, J. An, J. Hazard. Mater. 169 (2009) 546–550.
[4] L. Tang, J.J. Wang, G.M. Zeng, Y.N. Liu, Y.C. Deng, Y.Y. Zhou, J. Tang, J.J. Wang, Z. Guo, J. Hazard. Mater. 306 (2015) 295–304.
[5] Y. Cui, J. Huang, X. Fu, X. Wang, Catal. Sci. Technol. 2 (2012) 1396.
[6] H. Wang, X. Yuan, Y. Wu, G. Zeng, X. Chen, L. Leng, Z. Wu, L. Jiang, H. Li, J. Hazard. Mater. 286 (2015) 187–194.
[7] G. Zeng, Y. Liu, L. Tang, G. Yang, Y. Pang, Y. Zhang, Y. Zhou, Z. Li, M. Li, M. Lai, X. He, Y. He, Chem. Eng. J. 259 (2015) 153–160.
[8] J.L. Gong, B. Wang, G.M. Zeng, C.P. Yang, C.G. Niu, Q.Y. Niu, W.J. Zhou, Y. Liang, J. Hazard. Mater. 164 (2009) 1517–1522.
[9] L. Tang, G.M. Zeng, G.L. Shen, Y.P. Li, Y. Zhang, D.L. Huang, Environ. Sci. Technol. 42 (2008) 1207–1212.
[10] Y. Zhang, G.M. Zeng, L. Tang, D.L. Huang, X.Y. Jiang, Y.N. Chen, Biosens. Bioelectron. 22 (2007) 2121–2126.
[11] Y. Deng, L. Tang, G. Zeng, H. Dong, M. Yan, J. Wang, W. Hu, J. Wang, Y. Zhou, J. Tang, Appl. Surf. Sci. 387 (2016) 882–893.
[12] F. Hashemzadeh, A. Gaffarinejad, R. Rahimi, J. Hazard. Mater. 286 (2015) 64–74.
[13] C. Mondal, M. Ganguly, J. Pal, A. Roy, J. Jana, T. Pal, Langmuir 30 (2014) 4157–4164.
[14] X.J. Hu, J.S. Wang, Y.G. Liu, X. Li, G.M. Zeng, Z.L. Bao, X.X. Zeng, A.W. Chen, F. Long, J. Hazard. Mater. 185 (2011) 306–314.
[15] L. Wang, X. Li, W. Teng, Q. Zhao, Y. Shi, R. Yue, Y. Chen, J. Hazard. Mater. 244–245 (2013) 681–688.
[16] C. Hsu, S. Wang, Y. Tzhou, Environ. Sci. Technol. 41 (2007) 7907–7914.
[17] J. Zhang, H. Shen, X. Wang, J. Wu, Y. Xue, Chemosphere 55 (2004) 167–174.
[18] Q. Yang, H. Choi, Y. Chen, D.D. Dionysiou, Appl. Catal. B: Environ. 77 (2008) 300–307.
[19] A. Chen, G. Zeng, G. Chen, X. Hu, M. Yan, S. Guan, C. Shang, L. Lu, Z. Zou, G. Xie, Chem. Eng. J. 191 (2012) 85–94.
[20] L. Liu, F. Chen, F. Yang, Y. Chen, J. Crittenden, Chem. Eng. J. 181–182 (2012) 189–195.
[21] W.Z. Tang, C.P. Huang, Water Res. 29 (1995) 745–756.
[22] X. Zhang, P. Zhang, L. Wang, H. Gao, J. Zhao, C. Liang, J. Hu, G. Shao, Appl. Catal. B: Environ. 192 (2016) 17–25.
[23] D. Xiao, K. Dai, Y. Qu, Y. Yin, H. Chen, Appl. Surf. Sci. 358 (2015) 181–187.
[24] F. Chang, C. Li, J. Chen, J. Wang, J. Luo, Y. Xie, B. Deng, X. Hu, Superlattice. Micro. 76 (2014) 90–104.
[25] Y. Li, W. Cui, L. Liu, R. Zong, W. Yao, Y. Liang, Y. Zhu, Appl. Catal. B: Environ. 199 (2016) 412–423.
[26] L. Liu, L. Ding, Y. Liu, W. An, S. Lin, Y. Liang, W. Cui, Appl. Catal. B: Environ. 201 (2017) 92–104.
[27] Bo Sun, Ettireddy P. Reddy, P.G. Smirniotis, Environ. Sci. Technol. 39 (2005) 6251–6259.
[28] Hongxiang Fu, Gongxuan Lu, S. Li, J. Photoch Photobio B 114 (1998) 81–88.
[29] Q. Wang, X. Chen, K. Yu, Y. Zhang, Y. Cong, J. Hazard. Mater. 246–247 (2013) 135–144.
[30] R. Liang, F. Jing, L. Shen, N. Qin, L. Wu, J. Hazard. Mater. 287 (2015) 364–372.
[31] L. Shi, L. Liang, J. Ma, F. Wang, J. Sun, Catal. Sci. Technol. 4 (2014) 758.
[32] C. Dai, E. Qing, Y. Li, Z. Zhou, C. Yang, X. Tian, Y. Wang, Nanoscale 7 (2015) 19970–19976.
[33] L. Tang, Y.C. Deng, G.M. Zeng, W. Hu, J.J. Wang, Y.Y. Zhou, J.J. Wang, J. Tang, W. Fang, J. Alloy. Compd. 662 (2016) 516–527.
[34] S. Wang, D. Li, C. Sun, S. Yang, Y. Guan, H. He, Appl. Catal. B: Environ. 144 (2014) 885–892.
[35] F. He, G. Chen, Y. Yu, S. Hao, Y. Zhou, Y. Zheng, ACS Appl. Mater. Inter. 6 (2014) 7171–7179.
[36] Y. Cui, J. Zhang, G. Zhang, J. Huang, P. Liu, M. Antonietti, X. Wang, J. Mater. Chem. 21 (2011) 13032–13039.
[37] Q. Liu, T. Chen, Y. Guo, Z. Zhang, X. Fang, Appl. Catal. B: Environ. 193 (2016) 248–258.
[38] J. Ran, T.Y. Ma, G. Gao, X.-W. Du, S.Z. Qiao, Energy Environ. Sci. 8 (2015) 3708–3717.
[39] F. Shi, L. Chen, M. Chen, D. Jiang, Chem. Commun. 51 (2015) 17144–17147.
[40] C. Han, L. Ge, C. Chen, Y. Li, X. Xiao, Y. Zhang, L. Guo, Appl. Catal. B: Environ. 147 (2014) 546–553.
[41] Y.C. Deng, L. Tang, G.M. Zeng, J.J. Wang, Y.Y. Zhou, J.J. Wang, J. Tang, Y.N. Liu, B. Peng, F. Chen, J. Mol. Catal. A: Chem. 421 (2016).
[42] L. Liu, Y. Qi, J. Lu, S. Lin, W. An, Y. Liang, W. Cui, Appl. Catal. B: Environ. 183 (2016) 133–141.
[43] L. Shao, D. Jiang, P. Xiao, L. Zhu, S. Meng, M. Chen, Appl. Catal. B: Environ. 198 (2016) 200–210.
[44] Y. Zhou, L. Zhang, W. Huang, Q. Kong, X. Fan, M. Wang, J. Shi, Carbon 99 (2016) 111–117.
[45] P. Niu, L. Zhang, G. Liu, H.-M. Cheng, Adv. Funct. Mater. 22 (2012) 4763–4770.
[46] S. Zhang, J. Li, X. Wang, Y. Huang, M. Zeng, J. Xu, ACS Appl. Mater. Inter. 6 (2014) 22116–22125.
[47] Y.P. Zhu, T.Z. Ren, Z.Y. Yuan, ACS Appl. Mater. Inter. 7 (2015) 16850–16856.
[48] L. Liu, Y. Qi, J. Hu, Y. Liang, W. Cui, Appl. Surf. Sci. 351 (2015) 1146–1154.
[49] Y. Zhou, L. Zhang, X. Fan, B. Wang, M. Wang, W. Ren, J. Wang, M. Li, J. Shi, J. Mater. Chem. A 3 (2015) 3862–3867.
[50] S. Hu, L. Ma, J. You, F. Li, Z. Fan, F. Wang, D. Liu, J. Gui, RSC Adv. 4 (2014) 21657.
[51] Q. Lin, L. Li, S. Liang, M. Liu, J. Bi, L. Wu, Appl. Catal. B: Environ. 163 (2015) 135–142.
[52] L. Tang, Y. Fang, Y. Pang, G. Zeng, J. Wang, Y. Zhou, Y. Deng, G. Yang, Y. Cai, J. Chen, Chem. Eng. J. 254 (2014) 302–312.
[53] L. Tang, G.-D. Yang, G.-M. Zeng, Y. Cai, S.-S. Li, Y.-Y. Zhou, Y. Pang, Y.-Y. Liu, Y. Zhang, B. Luna, Chem. Eng. J. 239 (2014) 114–122.
[54] Y. Zhou, L. Tang, G. Yang, G. Zeng, Y. Deng, B. Huang, Y. Cai, J. Tang, J. Wang, Y. Wu, Catal. Sci. Technol. 6 (2016) 1930–1939.
[55] J. Xu, L. Zhang, R. Shi, Y. Zhu, J. Mater. Chem. A 1 (2013) 14766.
[56] Z. Lin, X. Wang, Angew. Chem. Int. Ed. 52 (2013) 1735–1738.
[57] J. Chen, Z. Hong, Y. Chen, B. Lin, B. Gao, Mater. Lett. 145 (2015) 129–132.
[58] X. She, H. Xu, Y. Xu, J. Yan, J. Xia, L. Xu, Y. Song, Y. Jiang, Q. Zhang, H. Li, J. Mater. Chem. A 2 (2014) 2563.
[59] S. Yang, Y. Gong, J. Zhang, L. Zhan, L. Ma, Z. Fang, R. Vajtai, X. Wang, P.M. Ajayan, Adv. Mater. 25 (2013) 2452–2456.
[60] J. Di, J. Xia, X. Li, M. Ji, H. Xu, Z. Chen, H. Li, Carbon 107 (2016) 1–10.
[61] H. Zhao, H. Yu, X. Quan, S. Chen, H. Zhao, H. Wang, RSC Adv. 4 (2014) 624–628.
[62] D. Xu, B. Cheng, S. Cao, J. Yu, Appl. Catal. B: Environ. 164 (2015) 380–388.
[63] J. Zhang, S. Liu, J. Yu, M. Jaroniec, J. Mater. Chem. 21 (2011) 14655.
[64] X. Hu, H. Ji, F. Chang, Y. Luo, Catal. Today 224 (2014) 34–40.
[65] J.-C. Wang, J. Ren, H.-C. Yao, L. Zhang, J.-S. Wang, S.-Q. Zang, L.-F. Han, Z.-J. Li, J. Hazard. Mater. 311 (2016) 11–19.
[66] T.-H. Liu, X.-J. Chen, Y.-Z. Dai, L.-L. Zhou, J. Guo, S.-S. Ai, J. Alloy. Compd. 649 (2015) 244–253.
[67] F. Li, Y. Dai, M. Gong, T. Yu, X. Chen, J. Alloy. Compd. 638 (2015) 435–442.
[68] X. Chen, Y. Dai, J. Guo, T. Liu, X. Wang, Ind. Eng. Chem. Res. 55 (2016) 568–578.
[69] G. Dong, L. Zhang, J. Phys. Chem. C 117 (2013) 4062–4068.